Fault-Tolerant Control Strategy of the Open-Winding Inverter for DC-Biased Vernier Reluctance Machines

Zixiang Yu, *Student Member, IEEE*, Wubin Kong, *Member, IEEE*, Dong Jiang, *Senior Member, IEEE*, Ronghai Qu, *Fellow, IEEE*, Dawei Li, *Member, IEEE*, Shaofeng Jia, *Member, IEEE*, Jianbo Sun, *Member, IEEE*, and Chun Gan, *Member, IEEE*

***Abstract*—This paper proposes a fault-tolerant control strategy of the open-winding inverter for dc-biased vernier reluctance machines (dc-biased VRMs), aiming to maintain the output capability after the open-circuit fault occurs in the inverter switches. DC-biased VRMs are with integrated winding current for both dc component for field excitation and ac component for torque generation. The torque generation is not associated with the current direction, making the full-bridge inverter be divided into two groups of devices. The proposed fault-tolerant control strategy is based on the regular full-bridge inverter for each open winding and can control the motor in the fault-tolerant mode with one group of devices. When an open-circuit fault of a device appears in the normal mode, the controller will switch to the fault-tolerant mode. After a short transient period, the motor will be able to work. Moreover, in the fault-tolerant mode, a pulsewidth modulation driving method is proposed to reduce the current ripple. The proposed method does not require any additional components, and the reliability of the drive control system with the open-winding inverter is improved. Experimental results verify the validity and feasibility of the proposed fault-tolerant control strategy.**

***Index Terms*—Control strategy, dc-biased, fault-tolerant, open-winding inverter, vernier reluctance machines (VRMs).**

I. Introduction

THE dc-biased vernier reluctance machine (dc-biased VRM) is developed from the stator wound field synchronous machine. Fig. 1(a) shows the topology of the dc-biased VRM, the machine combined the dc field winding and

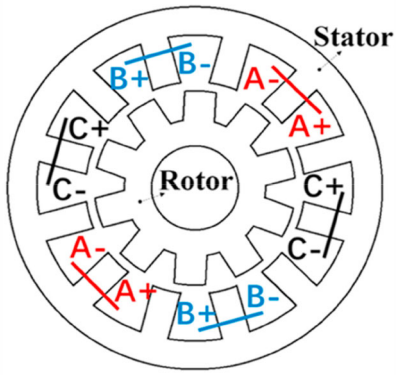

(a)

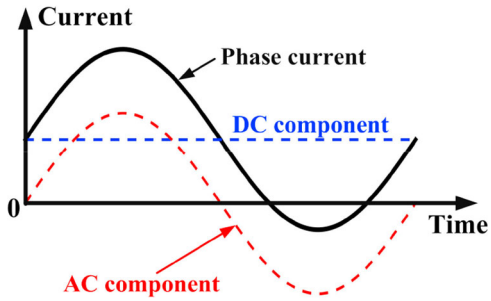

(b)

Manuscript received December 10, 2017; revised March 23, 2018; accepted May 1, 2018. Date of publication May 14, 2018; date of current version December 7, 2018. This work was supported in part by the National Natural Science Foundation of China under Grant 51607078, Grant 51607079, and Grant 51520105010; in part by the National Key Research and Development Program of China under Grant 2017YFB0102300 and Grant 2017YFB0102400; and in part by the Fundamental Research Funds for the Central Universities under Grant 2018KFYYXJJ070. Recommended for publication by Associate Editor A. K. Gupta. *(Corresponding author: Wubin Kong.)*

Z. Yu, W. Kong, D. Jiang, R. Qu, D. Li, and J. Sun are with the State Key Laboratory of Advanced Electromagnetic Engineering and Technology, School of Electrical and Electronic Engineering, Huazhong University of Science and Technology, Wuhan 430074, China (e-mail:

with the SRM drive system, the dc-biased VRM can be easily controlled in the synchronous rotating reference frame, a better control precision is guaranteed [10], [11]. The sinusoidal armature current also contributes to smaller torque ripple and vibration [12]. With these characteristics, the machine can be ideally used for traction applications requiring variable speed operation [13].

The power device is one of the vulnerable components among the drive control system [14]. According to a survey based on over 200 products from 80 companies, about 38% of faults in converters occur due to failures of power devices [15]. The power switches of the open-winding inverter are twice the quantity of the traditional three-phase inverter. Furthermore, since the current is asymmetric in positive and negative directions, the current stress in the power switches for conduction current in two directions will be different, and it makes the failure rate for the devices with larger stress to be higher. The characteristics reduce the reliability of the drive control system.

The power device failures can be classified into two cases: a short-circuit fault and an open-circuit fault [16]. A short-circuit fault occurs during the wrong gate voltage, overvoltage, and high temperature. It is difficult to handle and most of the existing insulated gate bipolar transistor (IGBT) short-circuit fault-tolerant controls are mainly through additional hardware circuits [17], [18]. An open-circuit fault occurs due to the lifting and cracking of bonding wires in the IGBT modules due to the thermal cycling. A gate drive fault is also one of the common causes of open-circuit faults. Compared with a short-circuit fault, an open-circuit fault does not cause serious damage, but it will reduce the system performance. It leads to current distortion and can cause secondary problems in other components through induced noise and vibrations. IGBT open-circuit failure can be with disattachment of die or wire-bond in the package of the module, which may be caused by high current, high temperature, or fatigue. In a typical IGBT module, the dies of IGBT and antiparalleled diodes can be with separate substrates. The failure of the IGBT may not impact much the antiparalleled diode. Therefore, utilization of the antiparalleled diode when the IGBT is with open-circuit failure is possible.

This paper proposes a novel fault-tolerant control strategy of the open-winding inverter for dc-biased VRMs, aiming to maintain the output capability after the open-circuit fault occurs in the inverter switches. The devices in the open-winding inverter can be divided into two groups: group 1 switches and group 2 switches. When an open-circuit fault happens in one group of devices, the inverter can switch to the other group of devices. Meanwhile, the antiparalleled free-wheeling diodes of the fault group are utilized to reconnect the phase windings and reconfigure the open-winding inverter into the asymmetrical half-bridge inverter. The operation principle of the dc-biased VRM is also analyzed, and a unidirectional current operation mode is associated with the reconfigured topology in order to maintain the output capability. Moreover, in the fault-tolerant mode, the two switches of the same phase are driven by the pulsewidth modulation (PWM) signal shifted by half-switching periods. Compared with the traditional PWM drive method without phase shift, the current ripple is reduced effectively.

Before actuation of the fault-tolerant control, fault detection and identification should be achieved. There are many fault identification methods for the IGBT open-circuit fault with current and voltage detection in the converter [19]–[21]. This paper mainly focuses on the fault-tolerant control method and the discussion on the fault identification method is little. But, it should be noticed that the fault identification speed is important for fault-tolerant control. Slower fault identification can degrade the fault-tolerant control performance.

The proposed fault-tolerant control strategy does not require any additional components, and the reconfigured topology also prevents the dc-bus shoot-through failure risk of the inverter. The reliability of the drive control system with the open-winding inverter is improved. This method can be helpful for several reliability critical applications that need the continuous operation. The drive system of the dc-biased VRM is introduced in Section II, open-circuit fault and fault-tolerant control are presented in Sections III and IV, with simulation results. Experimental results verify the validity and feasibility of the proposed fault-tolerant control strategy in Section V. Finally, conclusions are summarized in Section VI.

II. Drive System of the DC-Biased VRM

A. Drive System Topology

Fig. 1(a) shows the topology and stator currents of the 12-stator 10-rotor dc-biased VRM, the machine combined the dc field winding and the ac armature winding into the single stator winding. Thus, the phase currents are sinusoidal with dc bias, as shown in Fig. 1(b).

The three-phase currents of the dc-biased VRM are expressed as

$$\begin{cases} i_A = I_{ac}cos(\theta_e) + I_{dc} \\ i_B = I_{ac}cos(\theta_e - \gamma) + I_{dc} \\ i_C = I_{ac}cos(\theta_e + \gamma) + I_{dc} \end{cases} \tag{1}$$

where I_{ac} is the magnitude of the ac armature current component; θ_e is the electrical angle; I_{dc} is the dc-biased current in phase windings; γ is the electrical angle between different phases, and γ equals to $2\pi/3$. The stator flux is produced by the ac current component in the armature windings. Meanwhile, the rotor flux is flexibly changed by the dc-biased current. The average torque is produced by the interactions of the rotor flux and the stator flux.

Fig. 2 shows the topology of the dc-biased VRM drive system. The open-winding inverter with common dc bus is associated with the machine to produce the dc flow path, and the dc bus voltage is U_{dc}. The stator windings of the dc-biased VRM are connected by the output terminals of inverters 1 and 2. The whole inverter has 12 switches together with the antiparalleled diodes. The 12 switches are divided into two groups: Group 1 ($Sx1$ and $Sx4$, $x = a,\ b,\ c$ in this paper) and group 2 (Sx2 and Sx3). It is clear that group 1 devices will conduct the current in the arrow direction in Fig. 2, and group 2 devices will conduct the current in the reversed direction. This function determines

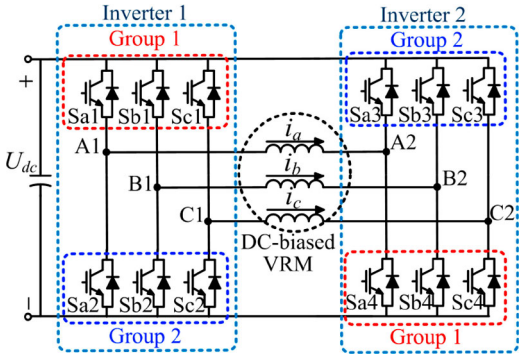

Fig. 2. Topology of the dc-biased VRM drive system.

the different roles for devices, and it is the hardware basis for the fault-tolerant control.

B. Operation Principle

The voltage equations for the dc-biased VRM in the synchronous rotating frame [6] are given by

$$\begin{bmatrix} u_d \\ u_q \\ u_0 \end{bmatrix} = R_s \begin{bmatrix} i_d \\ i_q \\ i_0 \end{bmatrix} + \begin{bmatrix} L_s & 0 & L_0 \\ 0 & L_s & 0 \\ L_0 & 0 & L_s + L_3 \cos 3\theta_e \end{bmatrix} \frac{d}{dt} \times \left(\begin{bmatrix} i_d \\ i_q \\ i_0 \end{bmatrix} \right) + \omega_e \begin{bmatrix} 0 & -L_s & 0 \\ L_s & 0 & L_0 \\ 0 & 0 & -3\omega_e L_3 \sin 3\theta_e \end{bmatrix} \begin{bmatrix} i_d \\ i_q \\ i_0 \end{bmatrix} \tag{2}$$

where u_d, u_q, and u_0 are $dq0$-axis voltages, and i_d, i_q, and i_0 are $dq0$-axis currents. L_s is the stator inductance, L_0 is the zero-axis inductance, and L_3 is the third self-inductance. R_s is the stator resistance, and ω_e is the electrical angular speed. In fact, i_0 is the dc-bias current used for field excitation, which does not exist in regular ac machine stator currents.

The cross-coupling component is the last term in (2), and the d-axis and q-axis flux are derived by the following:

$$\begin{cases} \phi_d = L_s i_d + L_0 i_0 \\ \phi_q = L_s i_q \end{cases} \tag{3}$$

where ϕ_d and ϕ_q are the d-axis and q-axis flux linkage, respectively.

Then, the mean torque is derived by the cross product of ϕ_d and ϕ_q. In the following equation, n_r is the number of rotor slots:

$$T_e = \frac{3}{2} n_r \left(\phi_d i_q - \phi_q i_d \right) = \frac{3}{2} n_r L_0 i_q i_0. \tag{4}$$

From (4), the average torque is related to the product of i_q and i_0. Meanwhile, if i_q and i_0 are controlled with the same polarity, the positive output torque will be generated. For example, if i_q and i_0 are both positive, or both negative, the output torque is exactly the same. In the constant torque operating region, the maximum torque per ampere control strategy is adopted [1], [4]. At the moment, $i_d = 0$, $i_q = i_{rms}$, $i_0 = 0.707 i_{rms}$, and i_{rms} is the root-mean-square (rms) value of phase currents. According to (4), the corresponding output torque is

$$T_{e\_MTPA} = \frac{3\sqrt{2}}{4} n_r L_0 {i_{rms}}^2. \tag{5}$$

It is clear that when i_q and i_0 are in the same direction, the torque can be controlled to be the same no matter the winding direction is positive or negative. Also, when the ac current amplitude is equal to the dc bias, the full current can be unidirectional. This is the basis for the proposed fault-tolerant control strategy.

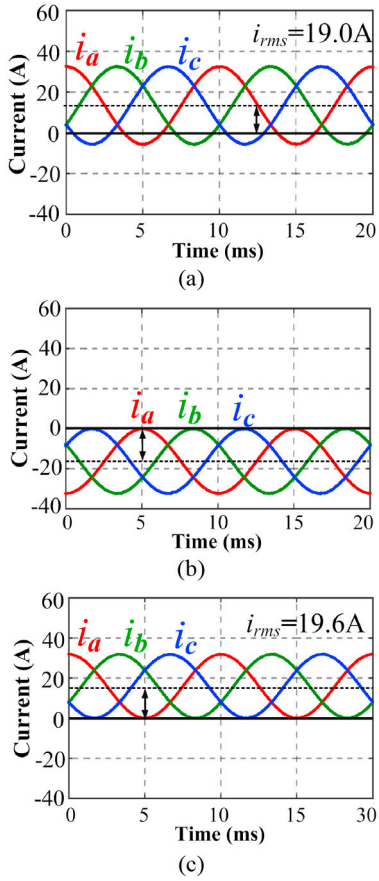

Fig. 3. Change of current waveforms. (a) Normal operating condition. (b) Fault-tolerant condition under group 1 switches' fault. (c) Fault-tolerant condition under group 2 switches' fault.

III. Open-Circuit Fault in the Open-Winding Inverter

When the drive system is operating under a normal condition, the phase current waveforms are shown in Fig. 3(a). The current waveforms passing through the group 1 switches are the positive part in Fig. 3(a), and the current passing through the group 2 switches is the negative part. Since the current is asymmetric in positive and negative directions, the current stress in the devices for conduction current in two directions will be different. The dc-biased current makes the group 1 switches to have a larger quantity of heat, and it makes the failure rate for the group 1 switches to be higher.

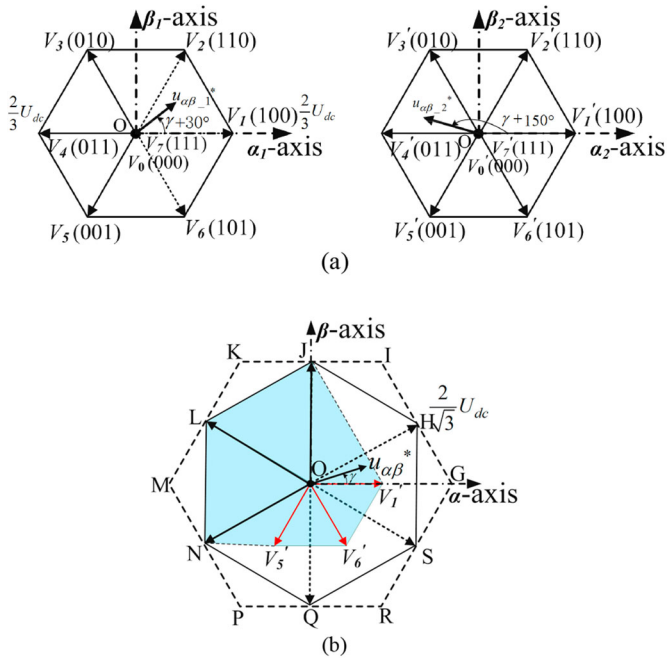

Fig. 4. Space voltage vector diagram of the open-winding inverter. (a) Individual voltage vectors for inverters 1 and 2. (b) Synthesized voltage vectors from the individual vectors.

The output voltage vector is synthesized by inverters 1 and 2, and the two inverters are driven by the space vector PWM (SVPWM) method. Fig. 4 shows the voltage vectors for the open-winding inverter. As shown in Fig. 4(a), the maximum voltage vector of inverters 1 and 2 for both is $2U_{dc}/\sqrt{3}$. In order to prevent the alternating common mode voltage, the voltage vector of inverter 2 leads inverter 1 by 120° electrical angle [25]. For example, $u_{\alpha\beta\_1}*$ leads $u_{\alpha\beta\_2}*$ by 120°. As shown in Fig. 4(b), the synthesized voltage vector $u_{\alpha\beta}*$ is solved by the subtraction of the two voltage vectors. Hence, the open-winding inverter has seven space voltage vectors, and they are located at the edges of H, J, L, N, Q, S, and O. The maximum value of the synthesized voltage vector is $2U_{dc}\sqrt{3}$. When an open-circuit fault of the open-winding inverter occurs, taking the fault occurring in switch Sa1, for example, as shown in the dotted line in Fig. 4(a), the voltage vectors V_1, V_2, and V_6 of inverter 1 become zero instead of $2U_{dc}/\sqrt{3}$.

In this instance, the synthesized voltage vectors of the open-winding inverters H, Q, and S are unachievable because of the lacking of voltage vectors in inverter 1. Instead, the synthesized voltage vectors depending on leg A become V_1', V_5', and V_6'. The modulation index is reduced to the shaded area shown in Fig. 4(b). The undesirable output voltage causes the distortion of output phase currents.

The fault condition is performed in MATLAB/Simulink. Fig. 5(a) shows the simulation results of output phase currents, phase voltage, and output torque under the Sa1 fault condition. The first stage is the normal condition, and the second stage is the faulty condition. When the open-circuit fault occurs, the positive current in phase A is unachievable. The above-mentioned undesirable output voltage also causes the current distortion in other phases. It leads to 132.3% torque ripple. Fig. 5(b) shows the simulation results under the Sa2 fault condition. The negative phase A current is unachievable, and the torque ripple is 12.3%. The torque ripple under the faulty condition causes secondary problems in noise and vibrations. The current flowing path under the faulty condition should be changed properly in order to maintain the output capability of the drive system.

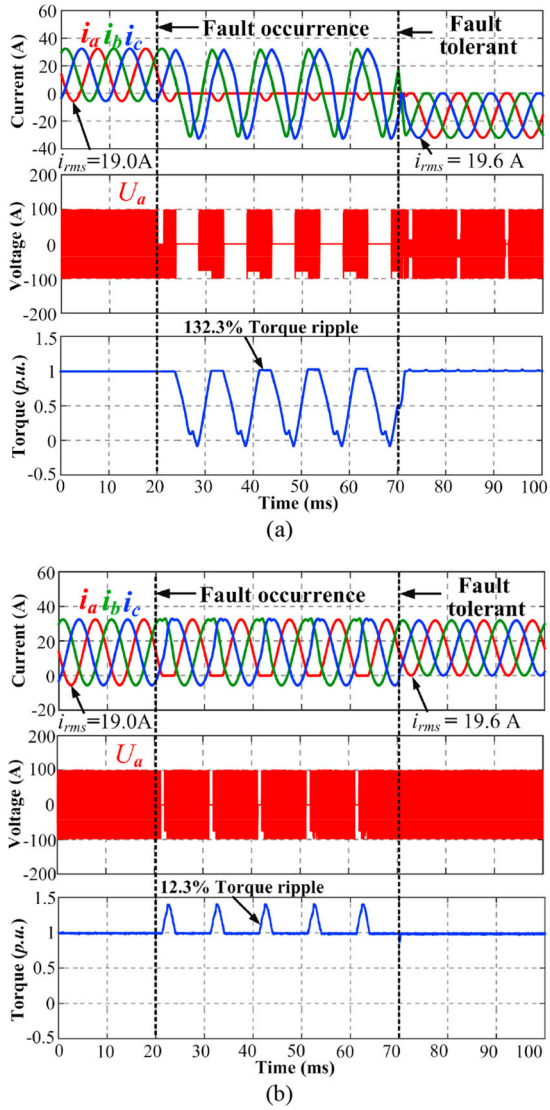

Fig. 5. Simulation results of phase currents, phase voltage, and output torque under (a) *Sa1* fault and (b) Sa2 fault.

IV. Proposed Fault-Tolerant Control Strategy

A. Operation of the Open-Winding Inverter Under the Open-Circuit Fault

The analysis is carried out considering two conditions: the faulty switches belong to group 1 (Sx1 and Sx4) or belong to group 2 (Sx2 and Sx3). The current that flows from input terminal 1 to output terminal 2 of the machine is the positive phase current $i_a > 0$ in this paper. The fault-tolerant control strategy is divided into two modes.

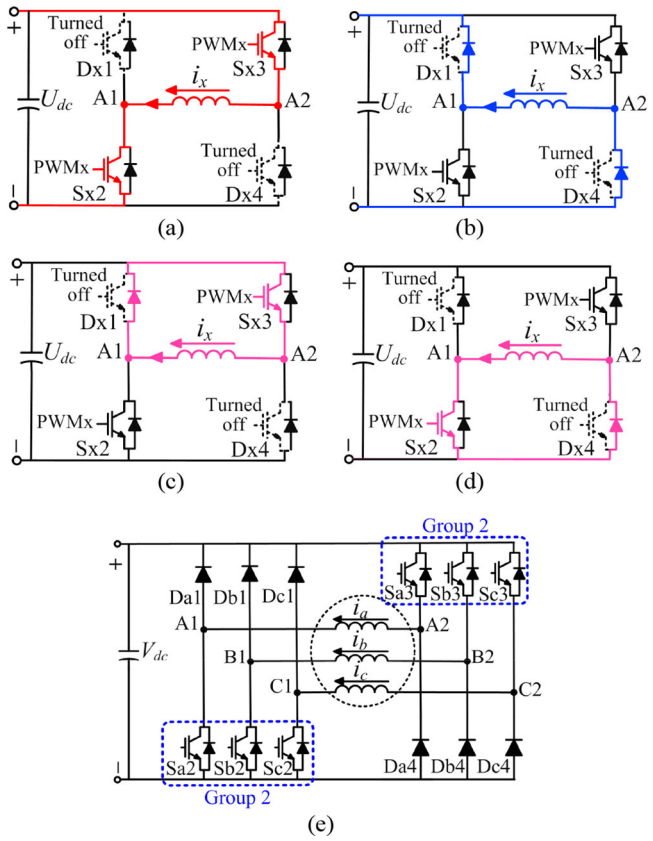

Fig. 6. Current flowing paths when the open-circuit fault occurs in group 1. (a) Phase current increase. (b) Phase current decrease. (c) Freewheeling state 1. (d) Freewheeling state 2. (e) Three-phase equivalent circuit.

Mode 1: Faulty switches belong to group 1 (Sx1 and Sx4).

When the open-circuit fault occurs in group 1, the low-level latching signals are applied to the gate pole of group 1 switches. All the six switches (Sx1 and Sx4) in group 1, including the faulty ones, are turned OFF. The corresponding antiparalleled freewheeling diodes (Dx1 and Dx4), together with the group 2 switches (Sx2 and Sx3), are utilized to provide the current flowing paths. The change of current flowing paths is shown in Fig. 6. It can be seen that the phase voltage has three states as following:

1) $+U_{dc}$, for the switching state (1 1);
2) $-U_{dc}$, for (0 0);
3) 0, for (1 0) and (1 1).

Fig. 6(a) indicates the current path when the phase current increases. At the moment, Sx2 and Sx3 are turned ON synchronously, and the switching state is (1 1). The output-pole voltage becomes $+U_{dc}$, and the phase currents increase. Fig. 6(b) denotes the current path when the phase current decreases. At the moment, Sx2 and Sx3 are turned OFF, and the switching state is (0 0). The phase currents flow through the freewheeling diodes Dx1 and Dx4. The output-pole voltage becomes $-U_{dc}$, and the phase currents decrease. Fig. 6(c) and (d) shows the freewheeling state. At the moment, only one switch is turned ON, and the other switch is turned OFF. The corresponding pole voltage is nearly 0. These four modes' combination is used for winding current control in mode 1.

The three-phase equivalent circuit is shown in Fig. 6(e). Because of the unidirectional characteristics of the antiparalleled diodes, the output currents are also unidirectional. The dc and ac components need further distribution. The negative dc-bias current is set equal to the amplitude of ac current, as shown in Fig. 3(b). At the moment, $i_d = 0, i_q = i_0 = -\sqrt{\frac{2}{3}} i_{rms}$. According to (4), the corresponding output torque is

$$T_{e\_\mathrm{Fault}} = n_r L_0 {i_{rms}}^2. \tag{6}$$

Compared with (5), the output torque remains in the same direction under the faulty condition. The output torque only reduces 5.7% under the same phase current rms value. What is more, the architecture in Fig. 6(e) is with only one IGBT in each phase leg, which means there is no dc-bus shoot-through failure risk in the inverter. The reliability of the drive system with the open-winding inverter is further improved.

The proposed control strategy is performed in MATLAB/Simulink. The third stage in Fig. 5(a) shows the fault-tolerant control under the Sa1 fault condition. The current distortion is eliminated and the currents become unidirectional. The negative unidirectional phase currents generate the same output torque. Meanwhile, torque ripple disappears and the machine operates stably.

Mode 2: Faulty switches belong to group 2 (Sx2 and Sx3).

When the open-circuit fault occurs in group 2, the low-level latching signals are applied to the gate pole of group 2 switches. All the six switches (Sx2 and Sx3) in group 2, including the faulty ones, are turned OFF. The corresponding antiparalleled freewheeling diodes (Dx2 and Dx3), together with the group 1 switches (Sx1 and Sx4), are utilized to provide the current flowing paths. The change of current flowing paths is shown in Fig. 7. The phase voltage also has three states: $+U_{dc}$, $-U_{dc}$, and 0.

Fig. 7(a) indicates the current path when the phase current increases. At the moment, Sx1 and Sx4 are turned ON synchronously, and the switching state is (1 1). The output-pole voltage becomes $+U_{dc}$, and the phase currents increase. Fig. 7(b) denotes the current path when the phase current decreases, and the switching state is (0 0). At the moment, Sx1 and Sx4 are turned OFF. The phase currents flow through the freewheeling diodes Dx2 and Dx3. The output-pole voltage becomes $-U_{dc}$, and the phase currents decrease. Fig. 7(c) and (d) shows the freewheeling state. At the moment, only one switch is turned ON, and the other switch is turned OFF. The corresponding pole voltage is nearly 0. These four modes' combination is used for winding current control in mode 2.

The three-phase equivalent circuit is shown in Fig. 7(e). Because of the unidirectional characteristics of the antiparalleled diodes, the output currents are also unidirectional. The dc and ac components need further distribution. The negative dc-bias current is set equal to the amplitude of ac current, as shown in Fig. 3(c). At the moment, $i_d = 0$, $i_q = i_0 = \sqrt{\frac{2}{3}} i_{rms}$. According to (4), the corresponding output torque is the same to (6). The output torque remains in the same direction under the faulty condition.

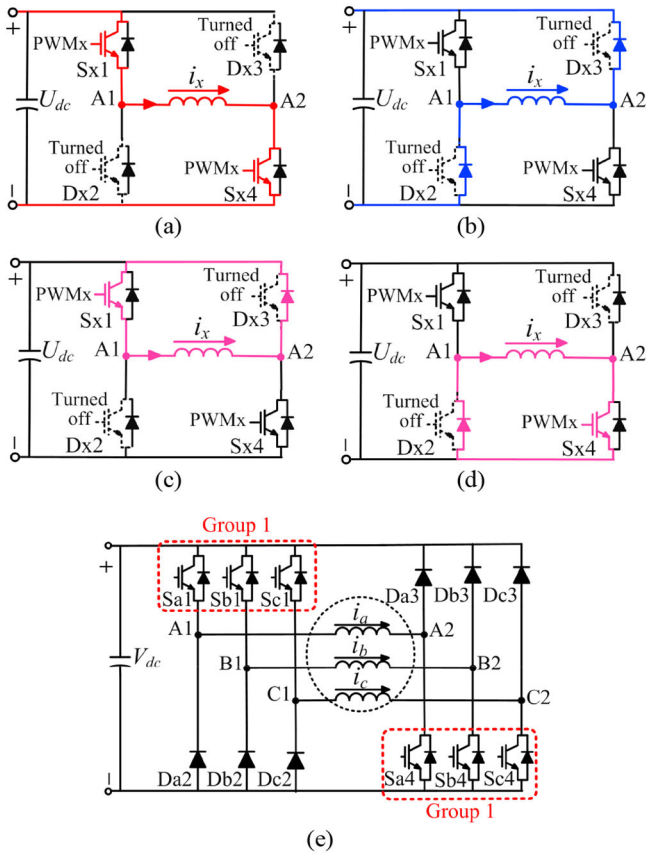

Fig. 7. Current flowing paths when the open-circuit fault occurs in group 2. (a) Phase current increase. (b) Phase current decrease. (c) Freewheeling state 1. (d) Freewheeling state 2. (e) Three-phase equivalent circuit.

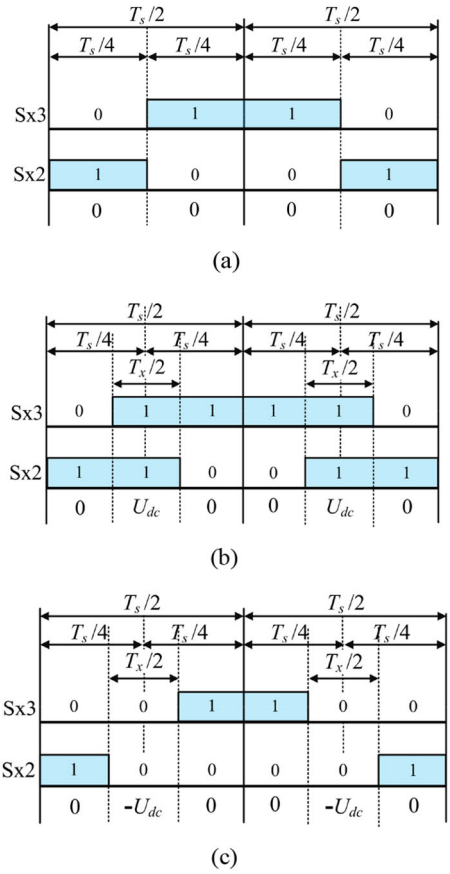

Fig. 8. Switching sequence for fault-tolerant control when (a) $T_x = 0$, (b) $T_x > 0$, and (c) $T_x < 0$.

The third stage in Fig. 5(b) shows the simulation results of the fault-tolerant control under the Sa2 fault condition. The current distortion is eliminated and the currents become unidirectional. The unidirectional phase currents generate the same output torque. Meanwhile, torque ripple disappears and the machine operates stably.

B. Modulation Method Under the Faulty Condition

When the drive system is operating under the normal condition, the voltage vector of inverter 2 leads that of the inverter 1 by 120 electrical angle. However, under the faulty condition, the two inverters are unable to produce the shifted voltages. Hence, the common mode voltage produced by the SVPWM method is inevitable. In the fault-tolerant mode, the sinusoidal PWM (SPWM) method is utilized to generate the unidirectional phase currents.

Fig. 8 shows the symmetrical switching sequence for fault-tolerant mode 1. The switching sequence for fault-tolerant mode 2 is exactly the same. T_x is the equivalent ON-time of phase voltages, and

$$T_x = u_x / U_{dc} \tag{7}$$

where u_x is the reference phase voltage applied to the phase winding, and $x = a, b, c$.

Fig. 8(a) shows the circumstance when $T_x = 0\,(x = a, b, c)$. It can be seen that Sx3 and Sx2 are driven by the PWM signal shifted by half-switching periods, and the duty cycle for both is 0.5. The purpose of the shifted PWM signal is to provide the freewheeling states (1 0) and (0 1), shown in Fig. 6(c) and (d), respectively. The current ripple will be much lower [23], [24]. Fig. 8(b) shows the circumstance when $T_x > 0$. The duty cycle of each PWM signal is increased by T_x / 2. The switching state (1 1) appears, shown in Fig. 6(a). It denotes the $+U_{dc}$ phase voltage with the switch ON time T_x. Fig. 8(c) shows the circumstance when $T_x < 0$. Compared with Fig. 8(a), the duty cycle of each PWM signal is reduced by T_x/ 2. The switching state (0 0) appears, shown in Fig. 6(b). It denotes the $-U_{dc}$ phase voltage with the switch ON time T_x. Compared with the normal condition, the maximum value of the phase voltage is also U_{dc}, and the voltage utilization ratio remains unchanged.

Although the SPWM method does not introduce the third-order common mode voltages [23], the back electromotive force (EMF) waveforms of the dc-biased VRM contain the third-order harmonics. The zero-axis harmonic voltages lead to the harmonic currents, and further cause torque ripple and energy loss. A zero sequence harmonic current suppression method is introduced.

According to the analysis mentioned above, the zero-sequence equivalent circuit of the open-winding dc-biased VRM

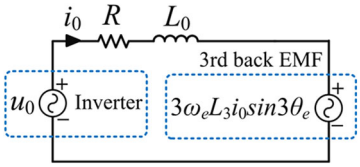

Fig. 9. Equivalent circuit of the dc-biased VRM drive system in the synchronous reference frame.

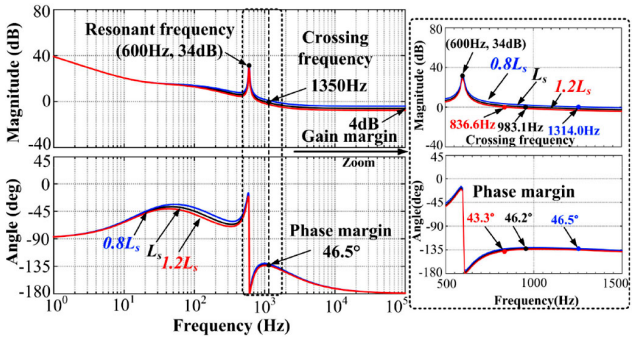

Fig. 10. Open-loop Bode diagram of the closed-loop current control strategy with PIR regulators when the parameter deviation is considered.

drive system is shown in Fig. 9, in which u_0 is the inverter output voltage, and $3\omega_e L_3 i_0 \sin 3\theta_e$ is the third-order back EMF generated by the dc-biased VRM. Thus, in order to suppress the zero-sequence current, the zero-sequence voltage reference should be modulated to counteract the third-harmonic component in back EMF.

Due to the limited ac signal tracking capability, the PI current regulator in synchronous rotating coordinate cannot eliminate the current distortion caused by the distorted EMF [25], [26]. The proportional integral and resonant (PIR) regulator is widely used in eliminating the alternating harmonic currents [27]. A current control strategy considering back EMF distortion using the PIR regulator in the zero-axis is illustrated. The forward transfer block $G_c(s)$ for a simple PIR controller is

$$G_c(s) = K_p + \frac{K_i}{s} + \frac{K_r s}{s^2 + \omega_0^2} \tag{8}$$

where K_p and K_i are the proportional and integral parameters of the PI part, K_r is the resonant parameter, and ω_0 is the resonance frequency. The open-loop transfer function of the PIR control loop is also defined from Fig. 10

$$\begin{aligned} G_{\text{open}}(s) &= G_{\text{sys}}(s) G_c(s) G_d(s) \\ &= \frac{K_p s^3 + (K_i + K_r) s^2 + K_p \omega_0^2 s + K_i \omega_0^2}{s(L_s s + R_s)(s^2 + \omega_0^2)} e^{-sT_d} \end{aligned} \tag{9}$$

where $G_d(s) = e^{-sT_d}$ is the digital control time delay caused by AD sampling. The control time delay T_d is selected as a sampling period 0.05 ms.

In order to suppress the third-order zero-sequence harmonic current of the dc-biased VRM drive system, the parameter design process of the PIR regulator needs to guarantee a phase margin around 45°. Meanwhile, the gain margin needs to be kept around 4–6 dB [28], [29]. Fig. 10 shows the open-loop Bode diagram of the closed-loop current control strategy with PIR regulators when the inductance parameter deviation is 20%. The parameters for the PIR regulator after the optimization are $K_p = 3.9$, $K_i = 300$, and $K_r = 3800$.

The resonance frequency of the PIR regulator changes with the motor speed (or current frequency). For the 12/10 dc-biased VRM, the pole pair number is 10. In order to eliminate the third-harmonic current in variable speed operations, the resonance frequency ω_0 (rad/ s) is set to π times the rotational speed (r/min). It changes closely with the rotational speed in order to assure the dynamic performance. Taking the speed at 1200 r/min, for example, the resonance frequency ω_0 is set as 1200π. As shown in Fig. 10, for a 600 Hz ac input signal, the open-loop gain of the PIR regulator is 34.0 dB. The open-loop gain at low frequency is 39.8 dB. It is large enough to eliminate the control error, and the accuracy of the current control can be guaranteed. The phase margin is 46.2° at 983.1 Hz when L_s is 596 μH, and the value decreases to 46.5° at 1314.0 Hz when the value is $0.8L_s$. When the value is $1.2L_s$, the crossing frequency is 836.6 Hz, and the corresponding phase margin is 43.3°. The degradation in the phase margin is harmful to the system stability. In order to ensure the stable closed-loop current control, the maximum inductance $1.2L_s$ is chosen as the design standard, and the stability is also guaranteed.

C. Overall Control Method

The control scheme for the dc-biased VRM drive system is shown in Fig. 11. Fig. 11(a) shows the normal mode, and Fig. 11(b) shows the fault-tolerant mode. The control diagram consists of one speed loop and three current loops. The phase current reference $i_{rms}*$ is given by a speed error through the PI regulator. The additional closed-loop current control with the PIR regulator is introduced in the zero-axis to alternating zero-axis harmonic current.

Fig. 12 shows the flowchart of the operation mode selection algorithm. When the machine is operating under the normal condition, it is driven by the SVPWM method. In order to prevent the alternating common mode voltage, the voltage vector of inverter 2 leads inverter 1 by 120° electrical angle [25], as shown in Fig. 11(a). When the open-circuit fault occurs in the switches, the low-level signal is applied to the gate pole of the six corresponding half-bridge switches. As shown in Fig. 11(b), all the six corresponding switches, including the faulty ones, are turned OFF by the latching signal. The corresponding antiparalleled freewheeling diodes, together with the other six half-bridge switches, are utilized to provide the current flow paths. Because of the unidirectional characteristics of the antiparalleled diodes, the output currents under fault-tolerant modes are also unidirectional. The dc and ac current components need further distribution. The dc component is set a little larger than the amplitude of the ac component to assure the unidirectional current.

V. Experimental Results

To verify the proposed fault-tolerant methods, the experiments have been performed based on the dc-biased VRM drive

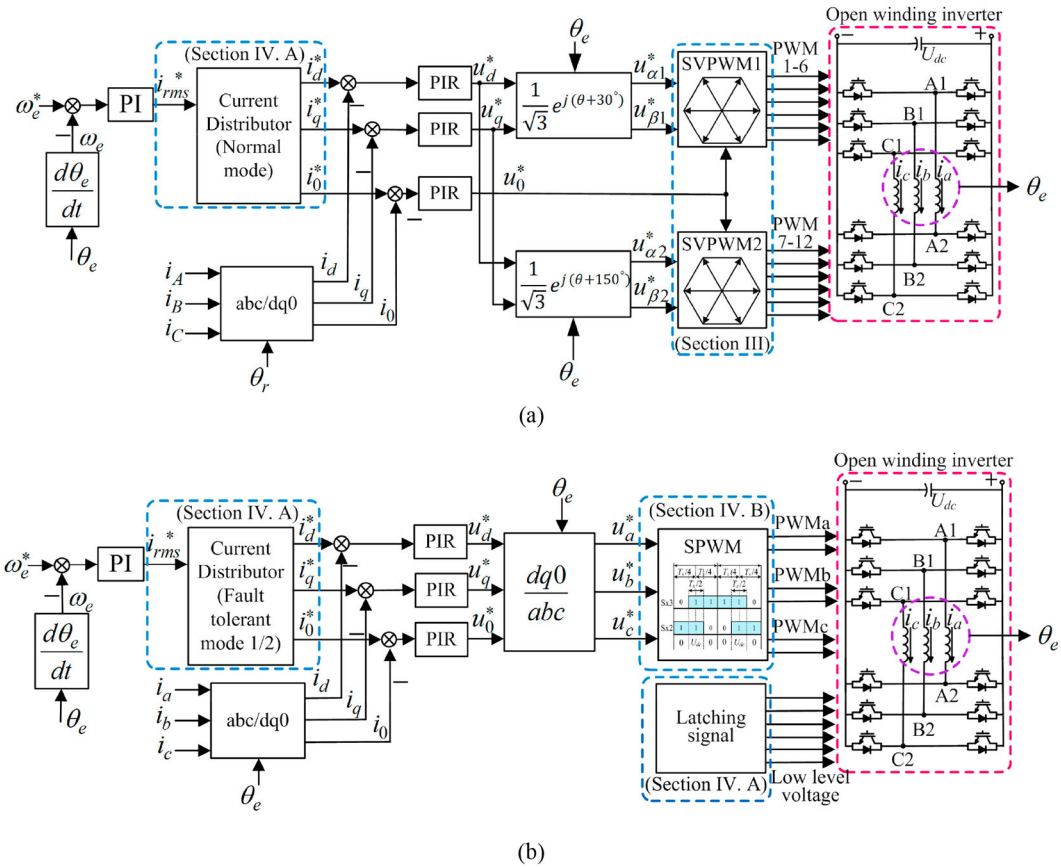

Fig. 11. Control block diagram of the dc-biased VRM drive control system under (a) normal mode and (b) fault-tolerant mode.

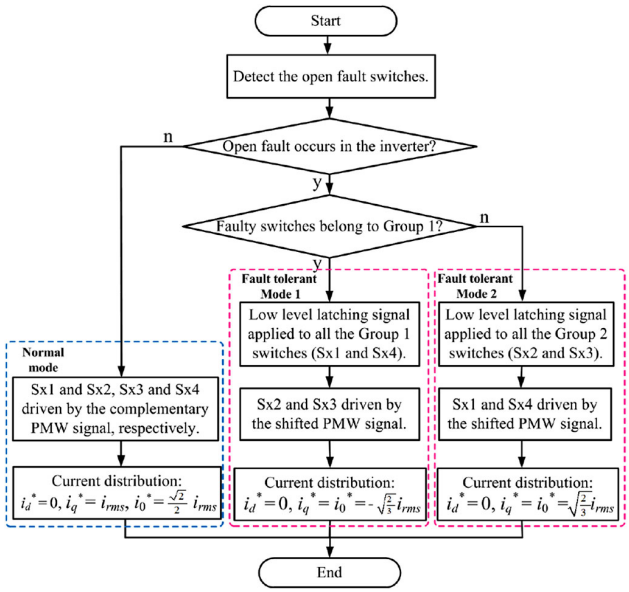

Fig. 12. Flowchart of the operation mode selection algorithm.

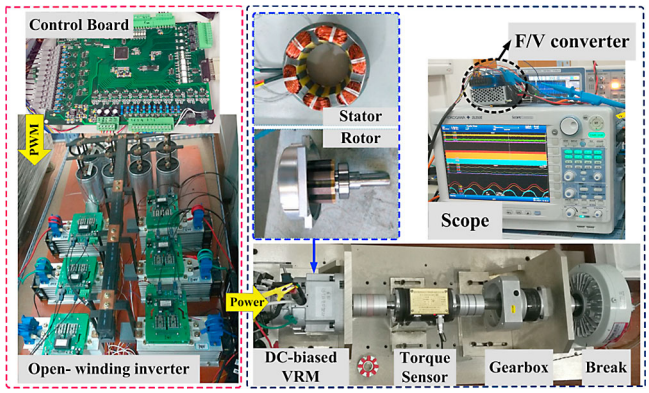

Fig. 13. Picture of the experimental setup.

system, with its picture shown in Fig. 13. The drive system includes an open-winding inverter with common dc bus, a prototype 12/10 open-winding dc-biased VRM, and a digital controller. The parameters of the machine are listed in Table. I. The digital controller is based on TMS320F28335 DSP. The sampling frequency and IGBT switching frequency are both 20 kHz. The output torque and output power are tested by a JN338 torque–speed sensor. The output signal for the torque–speed sensor is transformed by an *F/V* converter. All the experimental waveforms are captured from a Yokogawa DL850E multiple-channel oscilloscope.

A. Fault-Tolerant Operations

Fig. 14 shows the experimental results of the proposed fault-tolerant control strategy. The first stage is the normal condition,

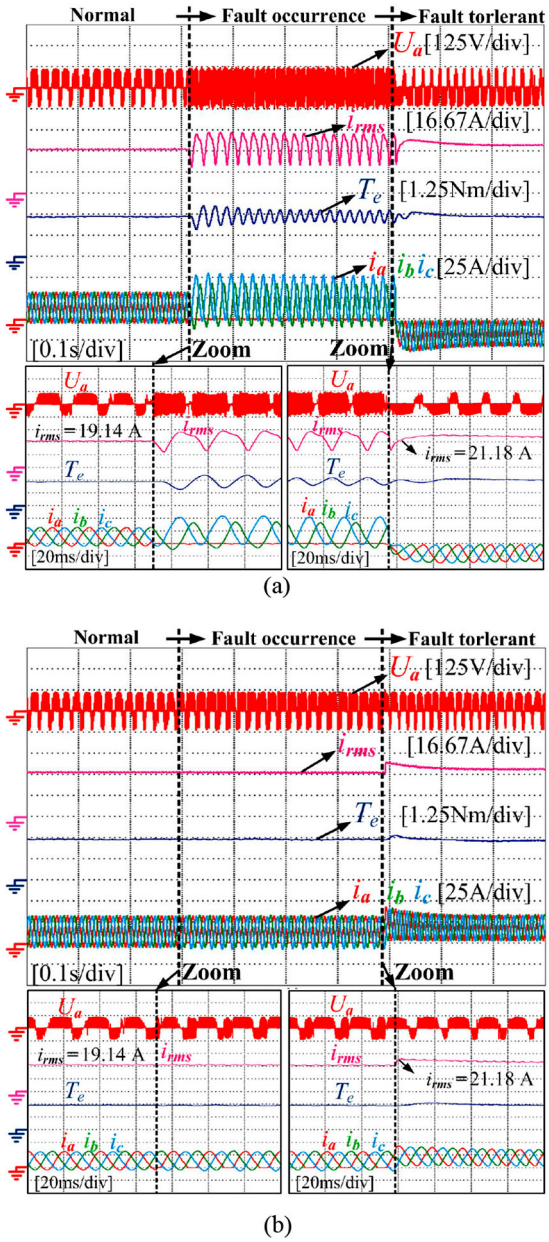

Fig. 14. Experimental results of the proposed method under (a) Sa1 fault and (b) Sa2 fault.

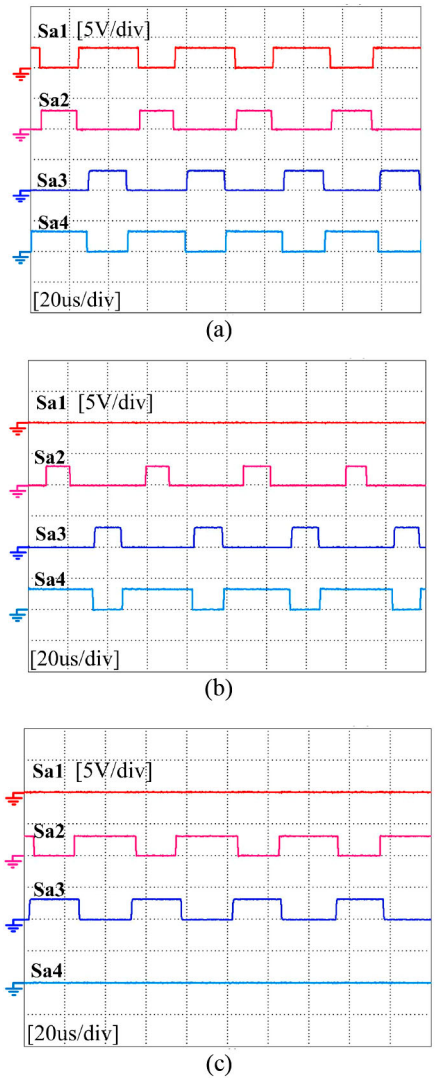

Fig. 15. PWM driving signals of phase A switches under (a) normal condition, (b) Sa1 fault condition, and (c) fault-tolerant mode 1.

the second stage is the faulty condition, and the third stage is the fault-tolerant operation state. Due to the limited resolution of the torque sensor, the operating speed is set to 300 r/min, and the corresponding load torque is the rated 2.2 Nm.

Fig. 14(a) shows the experimental results when the open-circuit fault occurs in Sa1. The Sa1 open fault occurs at the second stage, and as analyzed in Section III, the positive i_a is unachievable. The undesirable output voltage in Fig. 4 also causes the current distortion in other phases. The output currents are distorted and it leads to the torque ripple. The actual torque ripple waveform should be the same as the simulation results in Fig. 5(a), but the waveform was "filtered" due to the low resolution of a torque sensor. Hence, the torque ripple is smaller than the simulation results. After the implementation of the proposed fault-tolerant control strategy, the distortion is eliminated and the currents become unidirectional. The phase current rms value increased from 19.14 to 21.18 A. The torque ripple disappeared and the machine operates stably.

Fig. 14(b) shows the experimental results when the open-circuit fault occurs in Sa2. The negative i_a is unachievable, and it leads to the current distortion. After the implementation of the proposed fault-tolerant control strategy, the currents become positively unidirectional. Moreover, the phase current rms value is approximately equal to the value in Fig. 14(a). This indicates the two unidirectional currents generate the same output torque.

Fig. 15 shows the corresponding PWM driving signals of phase A switches under different conditions. Fig. 15(a) shows the normal condition, in which Sx1 and Sx2, Sx3 and Sx4 are driven by the complementary PWM signal. Fig. 15(b) shows the Sa1 fault condition. The open fault is realized by applying the OFF signal to the gate pole of Sa1. Fig. 15(c) shows the fault-tolerant condition. When the open-circuit fault occurs in the switches, the low-level signal is applied to the gate pole of

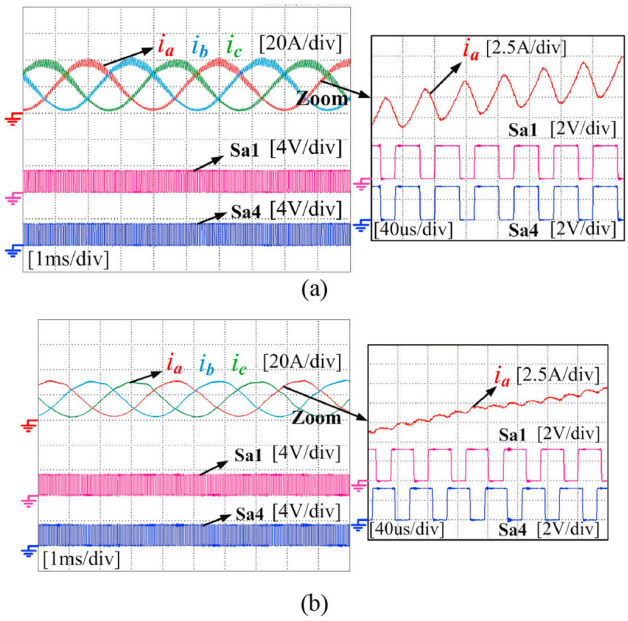

Fig. 16. Current waveforms and PWM driving signals of phase A switches under the faulty condition. (a) Sa1 and Sa4 driven by the traditional PWM signals. (b) Sa1 and Sa4 driven by the proposed PWM signals shifted by half-switching periods.

the six corresponding half-bridge switches. All the six corresponding switches, including the faulty ones, are turned OFF. Meanwhile, Sx2 and Sx3 are driven by the PWM signal shifted by a half-switching periods, as mentioned in Section IV-B. The corresponding antiparalleled freewheeling diodes, together with the other six half-bridge switches, are utilized to provide the current flowing paths.

Fig. 16 shows the current waveforms and PWM driving signals under the faulty condition in mode 2. The machine is operating with the rated 2.2 Nm load at the speed of 1500 r/min. In Fig. 16(a), Sa1 and Sa4 are driven by the traditional PWM signal without phase shift. It can be seen that Sa1 and Sa4 turned ON and turned OFF synchronously. As mentioned in Section IV-B, the switching states are (1 1) and (0 0). The lack of a freewheeling state leads to the 4.5 A current ripple in Fig. 16(a). In Fig. 16(b), Sa1 and Sa4 are driven by the proposed PWM signal shifted by half-switching periods. It can be seen that the phase current increases when the switching state is (1 1). Meanwhile, the freewheeling states (1 0) and (0 1) make the phase current decrease smoothly. The current ripple is 0.6 A in Fig. 16(b), and the value is much lower.

Fig. 17 shows the experimental comparisons between the zero-axis PI regulator and the zero-axis PIR regulator with the fault-tolerant strategy under mode 2. The load torque is set to 1.97 Nm, and the operation speed is 1200 r/min. The SVPWM method, together with the back EMF harmonics of the dc-biased VRM, introduces the common mode voltage harmonics. When the drive system is operating with the zero-axis PI regulator, the phase current i_a and the zero-axis current i_0 contain the third-order harmonic. The corresponding phase current rms value is 18.45 A. After applying the PIR regulator, the third-order harmonic current in the zero-axis is reduced to zero, and the A

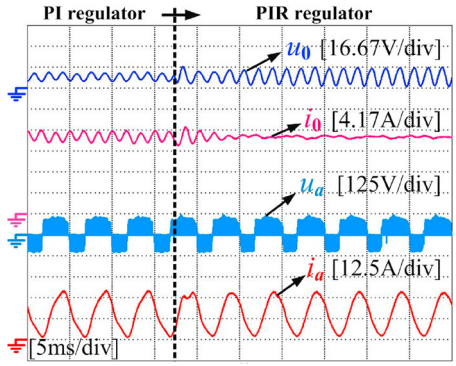

Fig. 17. Experimental comparisons between the zero-axis PI regulator and the zero-axis PIR regulator under the fault-tolerant condition of group 2.

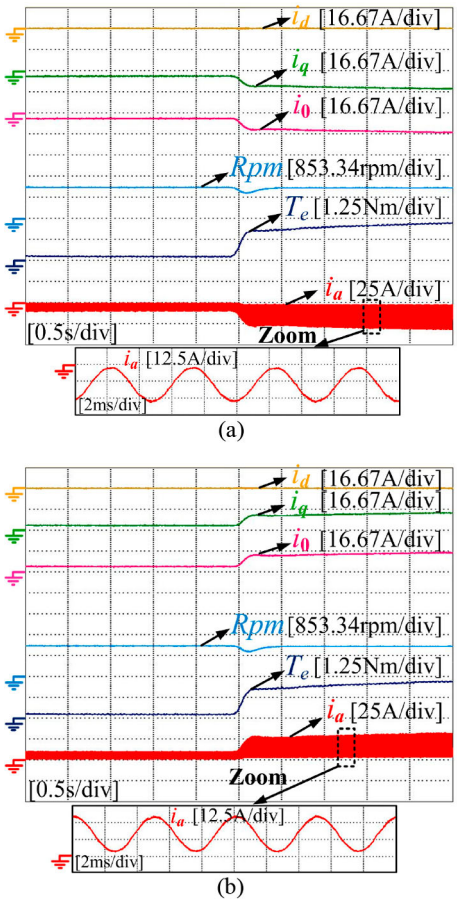

Fig. 18. Experimental results of the dynamic response when the load is changed from 0.12 to the rated 2.2 Nm with the proposed control strategy under (a) mode 1 and (b) mode 2.

phase current becomes nearly sinusoidal. The corresponding phase current rms value decreases to 18.07 A, and it contributes to lower energy loss. The PIR regulator in the zero-axis is necessary under the fault-tolerant condition.

B. Variable Torque and Speed Operations

Fig. 18 shows the dynamic response when the load is changed from 0.12 Nm to the rated 2.2 Nm at the speed of 1200 r/min.

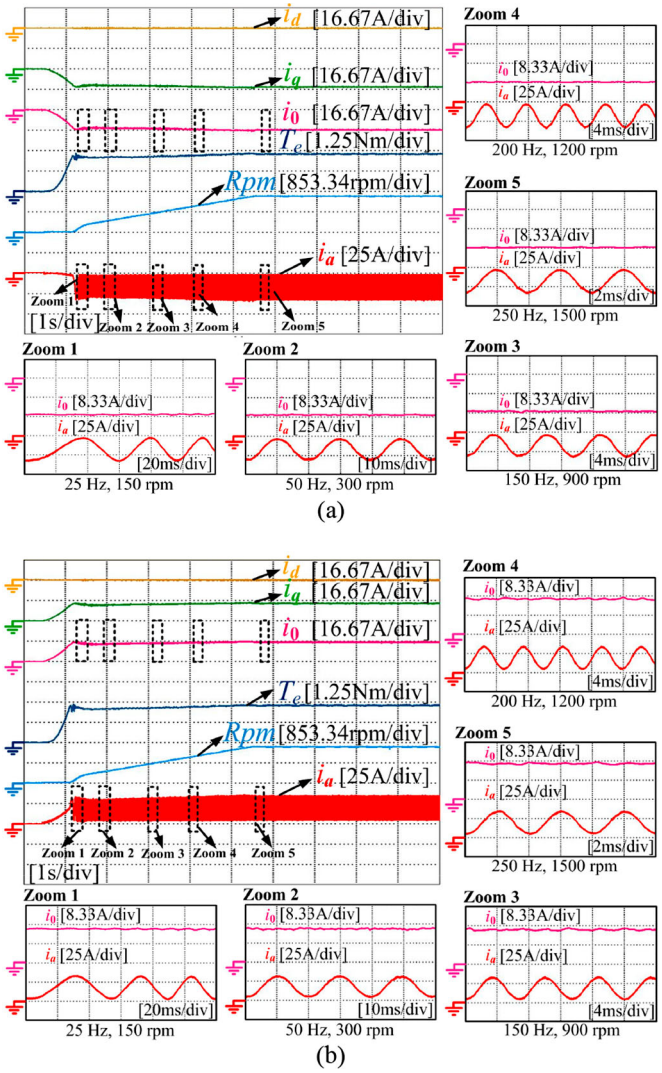

Fig. 19. Experimental results of the dynamic performance from standstill to 1500 r/min with the proposed method under (a) mode 1 and (b) mode 2.

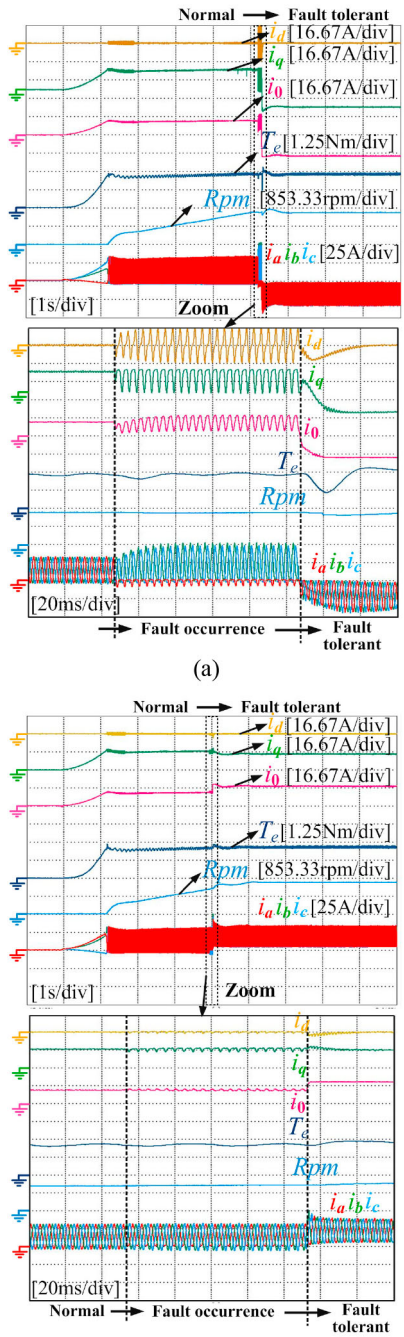

Fig. 20. Experimental results when the drive switches from normal operation to fault operation under (a) Sa1 fault and (b) Sa2 fault.

Fig. 18(a) shows the fault-tolerant operation state under mode 1. When the load is applied at 2.5 s, the speed controller generates more negative q-axis current and zero-axis current. The speed recovers within 0.3 s. The zero-axis current is a little larger than the q-axis current to assure the unidirectional phase current in the negative direction. The corresponding phase current rms value is 20.65 A with the negative phase current. Fig. 18(b) shows the fault-tolerant operation state under mode 2, and the load state is exactly the same. The q-axis current and zero-axis current are positive, and the corresponding phase currents are positive. The phase current rms value is 20.72 A. As mentioned in Section II-B, the same polarity of i_q and i_0 generates the positive torque, and it makes the same dynamic characteristics under the two conditions.

Fig. 19 shows the machine's $dq0$-axis currents, output torque, speed, and phase currents, when the machine accelerates from 0 to 1500 r/min with a 2.2 Nm rated load. The reference speed is applied as a ramp input, and the speed regulator tracks the reference speed well. Fig. 19(a) and (b) shows the fault-tolerant operation state under modes 1 and 2, respectively. The proposed fault-tolerant control strategy shows great dynamic responses under both the faulty conditions. Besides, from the five zoomed current waveforms in the two figures, the frequency of the fundamental current waveforms is 25, 50, 150, 200, and 250 Hz. The corresponding motor speed is 150, 300,

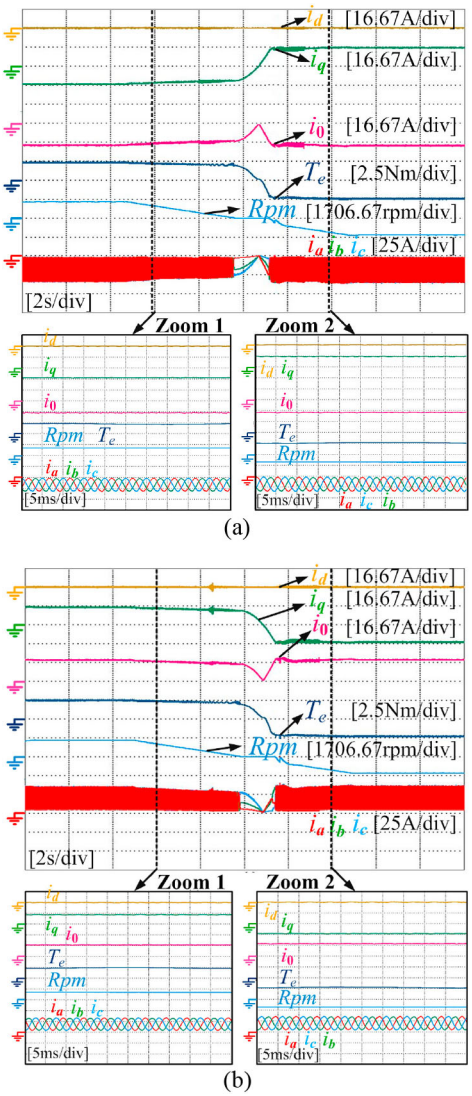

Fig. 21. Experimental results of the machine decelerate from 1500 to –1500 r/min with the proposed method under (a) mode 1 and (b) mode 2.

900, 1200, and 1500 r/min. Compared with the zero-axis current waveform in Fig. 17, the zero-axis currents are stable with the zero-axis PIR regulator. The phase currents are sinusoidal because the resonance frequency of the PIR regulator changes closely with the rotational speed. The third-order zero-axis harmonic currents are eliminated effectively in the variable speed operation.

Fig. 20 shows the transient process when the drive switches from normal operation to fault operation. The machine accelerates from 0 to 1500 r/min with a 2.2 Nm rated load. The reference speed is applied as a ramp input. In Fig. 20(a), the open-circuit fault occurs in Sa1 at the speed of 1440 r/min. The q-axis current and zero-axis current are both positive in normal operation before the open-circuit fault occurs. Hence, the positive torque is generated. After the implementation of the fault-tolerant control strategy, the q-axis current and zero-axis current are both negative. The same polarity of i_q and i_0 also generates the positive torque. In Fig. 20(b), the open-circuit fault occurs in Sa2 at the speed of 1171 r/min. After the implementation of the proposed fault-tolerant control strategy, the dc-bias current i_0 is set a little larger than i_q due to the unidirectional characteristic. The output capacity is also maintained in the transient process.

Fig. 21 shows the machine's $dq0$-axis currents, output torque, speed, and phase currents, when the machine decelerates from 1500 to –1500 r/min with a 2.2 Nm rated load. Fig. 21(a) and (b) shows the fault-tolerant operation state under modes 1 and 2, respectively. The reference speed is applied as a ramp input, and the speed regulator tracks the reference speed well. From the output torque equation (4), when the output torque is positive, the q-axis current i_q and the zero-axis current i_0 are with the same polarity. Hence, the machine rotates in the forward direction, and it shows the positive sequence in phase currents. The negative output torque is generated through changing the polarity of i_q. Hence, i_q and i_0 are with opposite polarity. The machine rotates in the reversed direction. It also shows the reversed sequence in phase currents.

VI. Conclusion

This paper has analyzed the open-circuit fault condition of the open-winding inverter for dc-biased VRMs. Based on the operation principle of dc-biased VRMs, a fault-tolerant control strategy for continuous operation with unidirectional currents is proposed. The proposed methods are explained by dividing the fault into two cases: the faulty condition of group 1 switches and group 2 switches. The proposed topology utilizes the antiparalleled free-wheeling diodes of the failed switches to reconnect the phase windings and reconfigures the open-winding inverter into the asymmetrical half-bridge inverter. Meanwhile, in the fault-tolerant mode, the two switches of the same phase are driven by the PWM signal shifted by half-switching periods. Compared with the traditional PWM drive method without phase shift, the current ripple is reduced effectively. Moreover, a zero sequence PIR regulator is introduced in order to suppress third-order common mode voltages.

The presented method allows the inverter operation with unidirectional output currents under an open-circuit fault condition, and it does not require any additional components and complex calculations. This method can be helpful for several safety critical applications that need the continuous operation. The reliability of the drive control system with the open-winding inverter is improved. Experimental results verify the validity and feasibility of the proposed fault-tolerant control strategy, and it shows great dynamic responses under both the faulty conditions. However, the proposed method is not suitable for the circumstance when one open-circuit fault occurs in group 1 switches and one open-circuit fault occurs in group 2 switches. Further study can be conducted to achieve the fault-tolerant control under the circumstance.

APPENDIX

TABLE I
PARAMETERS OF THE PROTOTYPE DC-BIASED VRM

Parameters	Symbol	Values
Stator slot number	n_s	12
Rotor slot number	n_r	10
Stator outer diameter (mm)	r_{os}	124
Rotor outer diameter (mm)	r_{or}	74.4
Axial length (mm)	l_a	105
Phase resistance (Ω)	R_s	0.088
Rated phase voltage (V)	u_{sN}	40
Rated phase current (A)	i_{sN}	19
Rated output torque (Nm)	T_{eN}	2.2
Output power @1500 rpm (W)	P_N	345

REFERENCES

[1] S. Jia, R. Qu, J. Li, and D. Li, "Flux modulation principles of dc-biased sinusoidal current vernier reluctance machines," in *Proc. IEEE Energy Convers. Congr. Expo.*, Sep. 2016, pp. 1–8.

[2] S. Jia, R. Qu, D. Li, J. Li, and W. Kong, "Improved torque capacity for flux modulated machines by injecting dc currents into the armature windings," *IEEE Trans. Magn.*, vol. 53, no. 6, Jun. 2017, Art. no. 8102205.

[3] S. Jia, R. Qu, J. Li, D. Li, and R. Zhang, "Stator/rotor slot and winding pole pair combinations of dc biased sinusoidal vernier reluctance machines," in *Proc. 22nd Int. Conf. Electr. Mach.*, Sep. 2016, pp. 904–910.

[4] Z. Yu *et al.*, "Optimal three-dimensional current computation flux weakening control strategy for dc-biased vernier reluctance machines considering inductance nonlinearity," *IEEE Trans. Power Electron.*, to be published.

[5] H. Zhan, Z. Q. Zhu, M. Odavic, and Y. Li, "A novel zero-sequence model-based sensorless method for open-winding PMSM with common dc bus," *IEEE Trans. Ind. Electron.*, vol. 63, no. 11, pp. 6777–6789, Nov. 2016.

[6] Z. Q. Zhu, B. Lee, and X. Liu, "Integrated field and armature current, control strategy for variable flux reluctance machine using open-winding," *IEEE Trans. Ind. Appl.*, vol. 52, no. 2, pp. 1519–1529, Mar./Apr. 2016.

[7] J. Kim, J. Jung, and K. Nam, "Dual-inverter control strategy for highspeed operation of EV induction motors," *IEEE Trans. Ind. Electron.*, vol. 51, no. 2, pp. 312–320, Apr. 2004.

[8] P. C. Kjaer, J. J. Gribble, and T. J. E. Miller, "High-grade control of switched reluctance machines," *IEEE Trans. Ind. Appl.*, vol. 33, no. 6, pp. 1585–1593, Nov./Dec. 1997.

[9] L. F. Chieh and S. M. Yang, "Self-bearing control of a switched reluctance motor using sinusoidal currents," *IEEE Trans. Power Electron.*, vol. 22, no. 6, pp. 2518–2526, Nov. 2007.

[10] N. Nakao and K. Akatsu, "Vector control specialized for switched reluctance motor drives," in *Proc. Int. Conf. Electr. Mach.*, Sep. 2014, pp. 937–943.

[11] Z. Q. Zhu and B. Lee, "Integrated field and armature current control for dual three-phase variable flux reluctance machine drives," *IEEE Trans. Energy Convers.*, vol. 32 no. 2, pp. 447–457, Jun. 2017.

[12] X. Liu *et al.*, "Performance comparison between unipolar and bipolar excitations in switched reluctance machine with sinusoidal and rectangular waveforms," in *Proc. IEEE Energy Convers. Congr. Expo.*, 2011, pp. 1590–1595.

[13] D. Li, R. Qu, and T. Lipo, "High-power-factor vernier permanent magnet machines," *IEEE Trans. Ind. Appl.*, vol. 50, no. 6, pp. 3664–3674, Nov./Dec. 2014.

[14] S. Yang, A. Bryant, P. Mawby, D. Xiang, L. Ran, and P. Tavner, "An industry-based survey of reliability in power electronic converters," *IEEE Trans. Power Electron.*, vol. 47, no. 3, pp. 1441–1451, May/Jun. 2011.

[15] S. Yang, D. Xiang, A. Bryant, P. Mawby, L. Ran, and P. Tavner, "Condition monitoring for device reliability in power electronic converters: A review," *IEEE Trans. Power Electron.*, vol. 25, no. 11, pp. 2734–2752, Nov. 2010.

[16] U. M. Choi, F. Blaabjerg, and K. B. Lee, "Reliability improvement of a T-type three-level inverter with fault-tolerant control strategy," *IEEE Trans. Power Electron.*, vol. 30, no. 5, pp. 2660–2673, May 2015.

[17] B. Lu and S. Sharma, "A literature review of IGBT fault diagnostic and protection methods for power inverters," *IEEE Trans. Ind. Appl.*, vol. 45, no. 5, pp. 1770–1777, Sep./Oct. 2009.

[18] M. Naidu, S. Gopalakrishnan, and T. W. Nehl, "Fault-tolerant permanent magnet motor drive topologies for automotive x-by-wire systems," *IEEE Trans. Ind. Appl.*, vol. 46, no. 2, pp. 841–848, Mar./Apr. 2010.

[19] R. Peuget, S. Courtine, and J. P. Rognon, "Fault detection and isolation on a PWM inverter by knowledge-based model," *IEEE Trans. Ind. Appl.*, vol. 34, no. 6, pp. 1318–1326, Nov./Dec. 1998.

[20] A. M. S. Mendes and A. J. Marques Cardoso, "Voltage source inverter fault diagnosis in variable speed ac drives, by the average current Park's vector approach," in *Proc. Int. Conf. Electr. Mach. Drives*, 1999, pp. 704–706.

[21] O. S. Yu, N. J. Park, and D. S. Hyun, "A novel fault detection scheme for voltage fed PWM inverter," in *Proc. IEEE Ind. Electron. Conf.*, 2006, pp. 2654–2659.

[22] M. R. Baiju, K. K. Mohapatra, R. S. Kanchan, and K. Gopakumar, "A dual two-level inverter scheme with common mode voltage elimination for an induction motor drive," *IEEE Trans. Power Electron.*, vol. 19, no. 3, pp. 794–805, May 2004.

[23] J. M. Erdman, R. J. Kerkman, D. W. Schlelgel, and G. L. Skibinski, "Effect of PWM inverters on ac motor bearing currents and shaft voltages," *IEEE Trans. Ind. Appl.*, vol. 32, no. 2, pp. 250–259, Mar./Apr. 1996.

[24] H. Makino and T. Kosaka, "Digital PWM-control-based active vibration cancellation for switched reluctance motors," *IEEE Trans. Ind. Appl.*, vol. 51, no. 6, pp. 4521–4530, Nov./Dec. 2015.

[25] H. Nian, Y. Zhou, and H. Zeng, "Zero-sequence current suppression strategy for open-winding PMSG fed by semicontrolled converter," *IEEE Trans. Power Electron.*, vol. 31, no. 1, pp. 711–720, Jan. 2016.

[26] M. Liserre, R. Teodorescu, and F. Blaabjerg, "Multiple harmonics control for three-phase grid converter systems with the use of PI–RES current controller in a rotating frame," *IEEE Trans. Power Electron.*, vol. 21, no. 3, pp. 836–841, May 2006.

[27] Y. S. Hu, Z. Q. Zhu, and K. Liu, "Current control for dual three-phase permanent magnet synchronous motors accounting for current unbalance and harmonics," *IEEE J. Emerging Sel. Topics Power Electron.*, vol. 2, no. 2, pp. 272–284, Jun. 2014.

[28] H. Nian and Y. Song, "Optimised parameter design of proportional integral and resonant current regulator for doubly fed induction generator during grid voltage distortion," *IET Renew. Power Gener.*, vol. 8, no. 3, pp. 299–313, Mar. 2014.

[29] D. G. Holmes, T. A. Lipo, B. P. McGrath, and W. Y. Kong, "Optimized design of stationary frame three phase ac current regulators," *IEEE Trans. Power Electron.*, vol. 24, no. 11, pp. 2417–2426, Nov. 2009.

Zixiang Yu (S'16) was born in Liaoning, China, in 1993. He received the B.E.E. degree in electrical engineering from Dalian Maritime University, Dalian, China, in 2015. He is currently working toward the M.S. degree at the School of Electronic and Electrical Engineering, Huazhong University of Science and Technology, Wuhan, China.

His current research interests include control strategy of permanent magnet machines, reluctance machines, and multiphase machines.

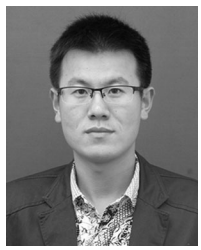

Wubin Kong (M'15) was born in Zhejiang, China, in 1986. He received the B.S. and Ph.D. degrees in electrical engineering from Zhejiang University, Hangzhou, China, in 2009 and 2014, respectively.

From 2015, he is a Lecture with the Huazhong University of Science and Technology, Wuhan, China. His research interests include high-power multiphase motor drives and fault-tolerant control motor drive applied in electric vehicles.

Dong Jiang (S'05–M'12–SM'16) received the B.S. and M.S. degrees in electrical engineering from Tsinghua University, Beijing, China, in 2005 and 2007, respectively. He began his Ph.D. study at the Center for Power Electronics Systems, Virginia Tech, Blacksburg, VA, USA, in 2007, and in 2010 with his advisor was transferred to the University of Tennessee, Knoxville, TN, USA, where he received the Ph.D. degree in power electronics and motor drives in 2011.

He was with the United Technologies Research Center, East Hartford, CT, USA, as a Senior Research Scientist/Engineer from January 2012 to July 2015. He has been with the Huazhong University of Science and Technology, Wuhan, China, as a Professor since July 2015. His major research interests include power electronics and motor drives, with more than 40 published IEEE journal and conference papers in this area.

Dr. Jiang was a recipient of two Best Paper Awards in IEEE conferences. He is an Associate Editor for the IEEE TRANSACTIONS ON INDUSTRY APPLICATIONS.

Ronghai Qu (S'01–M'02–SM'05–F'18) was born in China. He received the B.E.E. and M.S.E.E. degrees from Tsinghua University, Beijing, China, in 1993 and 1996, respectively, and the Ph.D. degree from the University of Wisconsin-Madison, Madison, WI, USA, in 2002, all in electrical engineering.

In 1998, he joined the Wisconsin Electric Machines and Power Electronics Consortiums as a Research Assistant. He became a Senior Electrical Engineer with Northland, a Scott Fetzer Company, in 2002. Since 2003, he has been with the General Electric (GE) Global Research Center, Niskayuna, NY, USA, as a Senior Electrical Engineer with the Electrical Machines and Drives Laboratory. He has authored more than 50 published technical papers and is the holder of more than 40 patents/patent applications. From 2010, he is a Professor with the Huazhong University of Science and Technology, Wuhan, China.

Dr. Qu has been a recipient of several awards from the GE Global Research Center since 2003, including the Technical Achievement and Management Awards, and also the 2003 and 2005 Best Paper Awards, third prize, from the Electric Machines Committee of the IEEE Industry Applications Society at the 2002 and 2004 Industry Applications Society Annual Meeting, respectively. He is a Full Member of Sigma Xi.

Dawei Li (S'12–M'15) was born in China. He received the B.E.E. degree from the Harbin Institute of Technology, Harbin, China, in 2010, and the Ph.D. degree from the Huazhong University of Science and Technology, Wuhan, China, in 2015, both in electrical engineering.

In July 2015, he joined the Huazhong University of Science and Technology. He has authored more than 60 published technical papers and is the holder of more than 10 patents/patent applications. His research interests include the design and analysis of flux-modulation permanent-magnet brushless machines.

Dr. Li was a recipient of the Best Poster Presentation Award from the XXIIth International Conference on Electrical Machines (2016), and Hubei Province Excellent Doctoral Dissertation (2016), China.

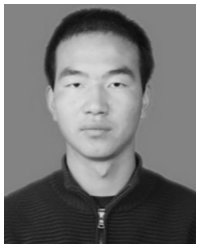

Shaofeng Jia (S'14–M'17) was born in Shaanxi, China. He received the B.Eng. degree from Xi'an Jiaotong University, Xi'an, China, in 2012, and the Ph.D. degree from Huazhong University of Science and Technology, Wuhan, China, in 2017, both in electrical engineering.

He is currently an Assistant Professor with the School of Electrical Engineering, Xi'an Jiaotong University. He is the Author/Co-Author of 30 IEEE technical papers. His research interests include design and analysis of novel permanent magnet and reluctance machines.

Jianbo Sun (M'01) was born in China. He received the B.Eng. and Ph.D. degrees in electrical engineering from Huazhong University of Science and Technology, Wuhan, China, in 2001 and 2005, respectively.

He is currently an Assistant Professor with the School of Electrical and Electronic Engineering, Huazhong University of Science and Technology. His research interests include design and analysis of novel permanent magnet machines, reluctance machines, and transformer.

Chun Gan (S'14–M'16) received the B.S. and M.S. degrees in power electronics and motor drives from China University of Mining and Technology, Jiangsu, China, in 2009 and 2012, respectively, and the Ph.D. degree in power electronics and motor drives from Zhejiang University, Hangzhou, China, in 2016.

He is currently a Research Associate with the Department of Electrical Engineering and Computer Science, The University of Tennessee, Knoxville, TN, USA. He is also a Member of the U.S. Energy/National Science Foundation cofunded Engineering Research Center for Ultra-Wide-Area Resilient Electric Energy Transmission Networks. He has authored or coauthored more than 40 technical papers in leading journals and conference proceedings, and authored one book chapter. He has ten issued/published invention patents. His research interests include high-efficiency power converters, electric vehicles, electrical motor drives, electrical motor design, continuous variable series reactor, high-voltage direct current transmission, and microgrid.

Dr. Gan was a recipient of the 2015 Top Ten Excellent Scholar Award, the 2016 Excellent Ph.D. Graduate, the 2015 Ph.D. National Scholarship, the 2015 Wang Guosong Scholarship, and the 2014 and 2015 Outstanding Ph.D. Candidate in Zhejiang University.